

See discussions, stats, and author profiles for this publication at: <https://www.researchgate.net/publication/224931289>

Dynamics of Local Chirality during SWCNT Growth: Armchair versus Zigzag Nanotubes

ARTICLE *in* JOURNAL OF THE AMERICAN CHEMICAL SOCIETY · MAY 2012

Impact Factor: 12.11 · DOI: 10.1021/ja301299t · Source: PubMed

CITATIONS

20

READS

39

4 AUTHORS:



Joonghan Kim

Catholic University of Korea

42 PUBLICATIONS 334 CITATIONS

SEE PROFILE



Alister J Page

University of Newcastle

57 PUBLICATIONS 643 CITATIONS

SEE PROFILE



Stephan Irle

Nagoya University

202 PUBLICATIONS 3,216 CITATIONS

SEE PROFILE



Keiji Morokuma

Fukui Institute for Fundamental Chemistry

439 PUBLICATIONS 13,611 CITATIONS

SEE PROFILE

Dynamics of Local Chirality during SWCNT Growth: Armchair versus Zigzag Nanotubes

Joonghan Kim,^{†,¶} Alister J. Page,^{†,¶} Stephan Irle,^{*,‡} and Keiji Morokuma^{*,†,§}

[†]Fukui Institute for Fundamental Chemistry, Kyoto University, Kyoto 606-8103, Japan

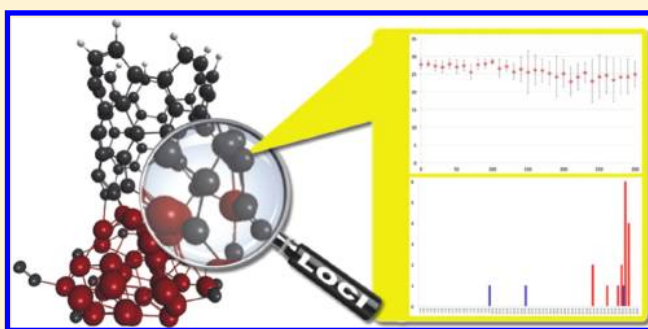
[‡]Department of Chemistry, Graduate School of Science, Nagoya University, Nagoya 464-8601, Japan

[§]Cherry L. Emerson Center for Scientific Computation and Department of Chemistry, Emory University, Atlanta, Georgia 30322, United States

Supporting Information

ABSTRACT: We present an analysis of the dynamics of single-walled carbon nanotube (SWCNT) chirality during growth, using the recently developed local chirality index (LOCI) method [Kim et al. *Phys. Rev. Lett.* 2011, 107, 175505] in conjunction with quantum chemical molecular dynamics (QM/MD) simulations. Using (5,5) and (8,0) SWCNT fragments attached to an Fe₃₈ catalyst nanoparticle, growth was induced by periodically placing carbon atoms at the edge of the SWCNT. For both armchair and zigzag SWCNTs, QM/MD simulations indicate that defect healing—the process of defect removal during growth—is a necessary, but not sufficient, condition for chirality-controlled SWCNT growth.

Time-evolution LOCI analysis shows that healing, while restoring the pristine hexagon structure of the growing SWCNT, also leads to changes in the local chirality of the SWCNT edge region and thus of the entire SWCNT itself. In this respect, we show that zigzag SWCNTs are significantly inferior in maintaining their chirality during growth compared to armchair SWCNTs.



1. INTRODUCTION

Potential electronic and optical applications of single-walled carbon nanotubes (SWCNTs)^{1,2} have remained elusive to date.³ This is due in large part to a lack of synthesis techniques allowing diameter- and chirality-controlled SWCNT growth, since it is these structural parameters that solely determine the electronic, optical, and mechanical properties of SWCNTs. To date, the production of a SWCNT “forest” consisting of a single, arbitrary (*n,m*) species of nanotube has not been reported in the literature. The solution to this problem arguably constitutes the forefront of carbon nanotube growth research. An understanding of the various aspects of chirality-controlled growth, such as the factors necessary to initiate, maintain, and influence SWCNT chirality, is therefore paramount if chirality-controlled SWCNT growth is to be achieved.

A number of attempts to this end have been reported in the literature thus far. Roughly speaking, traditional approaches toward chirality-controlled growth fall into either “catalyst design” or “postsynthesis” approaches (recently reviewed in refs 4 and 5). The former assumes that chirality-control may be attained by the optimization of the supporting catalyst nanoparticle and/or synthetic conditions. On the other hand, in the latter approach SWCNTs are synthesized using existing methods (such as catalytic chemical vapor deposition (CCVD),^{6,7} carbon-arc,^{1,2,8} or laser evaporation^{9,10}), after which postsynthesis processing is employed to refine the distribution of (*n,m*) SWCNTs in the sample. More novel

approaches include “amplification growth” (growth from oxidatively opened SWCNTs with preselected chirality, conceived originally by Smalley and co-workers^{11,12}) and “SWCNT cloning” (growth without docking, performed by Liu and co-workers¹³). The former method uses an iron catalyst, ethanol/ethylene feedstock, and growth temperatures between 700 and 850 °C, whereas the latter employs similar growth conditions to those for the catalyst-free, C₆₀-cap templated growth with a 20:1 CH₄/C₂H₄ feedstock mixture and a growth temperature of 975 °C. Although both methods were able to regrow existing SWCNTs to some extent, it was never shown that the regrown sidewalls precisely matched the chirality of the seed tube. Most recently, the use of organic-synthetic approaches to achieve chirality-controlled growth has been suggested. Scott and co-workers suggest that SWCNT growth in this case is driven by repeated Diels–Alder cycloaddition of acetylene onto the [*n*]cycloparaphenylenes ([*n*]CPPs), which correspond to a single layer of an armchair SWCNT.¹⁴ Other recent theoretical investigations¹⁵ also point to the possibility of a radical C₂H-based growth process from [*n*]CPPs. No experimental report of SWCNT in this manner has been reported to date. However, following the recent organic synthesis of CPPs corresponding to both armchair¹⁶ and chiral¹⁷ SWCNT templates, and even more recently of

Received: February 17, 2012

$C_{50}H_{10}$ – an entire extended (5,5) SWCNT cap structure¹⁸ – it is possible that such an approach may be a viable, low-temperature alternative to chirality-controlled growth.

In this work, we present the first ever analysis of the dynamics of local SWCNT chirality during the growth process. The chirality of SWCNT structures “grown in the computer” as the result of nonequilibrium MD simulations, has been estimated in the past.^{19–21} Such approaches have inevitably been based on defining both the edge structure and the diameter of the growth SWCNT structure, to estimate the (n,m) indices. However, the structural nature of these SWCNT caps necessarily imparts a degree of arbitrariness into such approaches. To this end, we employ the recently developed “local chirality index” (LOCI) method²² of calculating the local chiral angle, θ , of each constituent hexagon in the growing SWCNT. This approach is based on the relationship between the individual hexagons and the principal (i.e., growth) axis of the SWCNT itself, and thus, it has a sound physical basis. We employ quantum chemical molecular dynamics (QM/MD) simulations to model CVD growth of (5,5)-armchair and (8,0)-zigzag chirality SWCNT fragments on Fe_{38} nanoparticles. Moreover, we will discuss the role of pertinent environmental factors, such as the rate of carbon supply during the growth process, on chirality control. We believe that these simulations are the first aimed at addressing the impact of (n,m) SWCNT chirality on the defect-healing process. These simulations serve to indicate possible ways in which the local and, hence, global SWCNT chirality may be conserved during the growth process.

2. COMPUTATIONAL DETAILS

2.1. QM/MD Simulation of SWCNT Growth. Our simulations of SWCNT growth presented here are a direct extension of those reported previously by our group.²³ Thus, we will only briefly review our model systems and nonequilibrium QM/MD methodology here. We employ the self-consistent-charge density-functional tight-binding method²⁴ (SCC-DFTB) in conjunction with Newtonian molecular dynamics (MD) techniques. Hence, while the nuclear positions and velocities were described classically (and updated using the popular velocity–Verlet algorithm²⁵), the electronic potential between all atoms was described quantum mechanically. This potential was evaluated “on-the-fly” at each MD iteration. The DFTB parameters describing interactions between Fe, C, and H atoms employed here are those developed previously within our group.²⁶ A finite electronic temperature, T_e , of 10,000 K was enforced on the wave function throughout these simulations. As we have shown previously,²³ the benefit of a finite T_e is 2-fold: first, it decreases the melting-point of transition metal catalyst nanoparticles, which in the current context increases the rate of diffusion of carbonaceous species on the nanoparticle surface, thereby making it more reactive; second, it improves dramatically the convergence of the DFTB equations at each iteration of the MD simulation. The nuclear temperature was maintained at 1500 K for all simulations reported here using the Nosé–Hoover chain thermostat (chain length 3).²⁷ SWCNT growth was induced by supplying lone carbon atoms to the SWCNT–catalyst interface at regular intervals. The SWCNT–catalyst interface was defined as those carbon atoms having either sp-hybridization or a C–Fe bond. The position of each incoming carbon atom was then defined as follows: by defining the vector connecting a randomly chosen “target” edge atom and the center of mass of all target atoms, a point (O) was chosen 4 Å away from the SWCNT–catalyst complex; the initial position of the incoming carbon atom was then defined randomly in a sphere of radius 3 Å using polar coordinates (r, θ, ϕ) ; the velocity of the incoming carbon atom was then set at 1500 K along the vector connecting the chosen “target” edge atom, the center of mass of all target atoms, and the point O (see ref 28 for further details). Two supply intervals have been employed here, 1 C/0.5 ps

(“fast”) and 1 C/10 ps (“slow”). On a previous occasion,^{23,29} we have compared the SWCNT growth attained using these two supply rates in the context of chirality-control and demonstrated that defect-healing is dramatically improved using slower carbon supply rates. For each starting model system (described below) and each carbon supply rate, 10 QM/MD trajectories were computed (referred to using “ $(n,m)_{fast/slow} - x$ ”, where $x = A - J$); the results reported here therefore correspond to a total of 40 trajectories. We have previously employed³⁰ an identical approach to that employed here (i.e., 10 trajectories) and reported growth rates of 3.54 and 7.3 Å/ps, respectively, with 95% confidence intervals of 1.59 and 1.64 Å/ps. Therefore, despite a limited number of trajectories, we believe that 10 trajectories provide reasonable statistics of SWCNT growth. For each trajectory, initial velocities for all atoms were defined using a Maxwell–Boltzmann distribution at 1500 K, thus making each trajectory statistically independent from all others. Our model systems are similar to those employed previously²³ and are shown in Figure S1 in the Supporting Information (SI). We present here SWCNT growth simulations using (5,5)-armchair and (8,0)-zigzag SWCNT fragments. The catalyst particle employed here is an Fe_{38} cluster possessing the fcc structure of γ -iron (which is the most stable at 1500 K, compared to the bulk α - and δ -phases). Following the geometry optimization of the SWCNT– Fe_{38} complex, each of the 10 QM/MD trajectories was equilibrated thermally at 1500 K for 10 ps prior to the addition of carbon atoms to the system. The polygonal carbon ring populations of all trajectories are shown in SI Figures S2–S5.

2.2. The LOCI Method: Analysis of Local SWCNT Chirality.

We have recently developed the LOCI method to determine the local chirality of arbitrary SWCNTs,²² and we refer the reader to this reference for the full details of the method. Here we describe only briefly how the local chirality of constituent hexagons can be determined using the LOCI method. The code will become available shortly on our group website.³¹

For a growing, straight SWCNT structure, the principal axes (PAs), denoted as the *global* PAs (GPAs), may be calculated trivially. The *z*-component of the GPAs (GPAZ) is then assumed to be parallel to the growth axis of the SWCNT itself. We note here that if this assumption does not hold (i.e., if GPAZ and the growth axis are not approximately parallel), then the applicability of the LOCI method is limited, and a more involved methodology is required to determine GPAZ. Each constituent hexagon in the SWCNT structure is then identified, and its individual PAs, denoted as the *local* PAs (LPAs), are calculated. The angle (ϕ) between GPAZ and the *z*-axis of each hexagon’s LPAs (LPaZ) can then be used to determine the efficacy of the LOCI method for each hexagon. Hexagons with $\phi = 90^\circ$ (i.e. the plane of the hexagon is parallel to the growth axis of the SWCNT) are ideally suited to the LOCI method, whereas those with $\phi = 0^\circ$ (i.e., the plane of the hexagon is perpendicular to the growth axis of the SWCNT, such as in a cap) are not. All hexagons in the sidewall of an *ideal* SWCNT are categorized as the former. Intermediate cases (hexagons with ϕ between 0 and 90°) may be transformed to the suitable hexagon *via* two consecutive Euler rotations. Having done so, three angles (θ_1 , θ_2 , and θ_3) formed between the planes defined by GPAZ and three pairs of *para* carbon atoms in the hexagon are calculated. The effective average, θ ($\theta = [\theta_1 + \theta_2 + \theta_3]/3 - 60$),²² of θ_1 , θ_2 , and θ_3 is denoted as the *local chiral angle*. By definition, $0^\circ \leq \theta \leq 30^\circ$, and the overall chirality of a SWCNT can be described using a distribution of all constituent local chiral angles. For an ideal zigzag SWCNT, a single peak at $\theta = 0^\circ$ is observed, whereas for an ideal armchair SWCNT, a single peak at $\theta = 30^\circ$ is observed. The LOCI method has recently been applied successfully to ideal, as well as “irregular”, SWCNTs (i.e., those observed during the SWCNT growth process).²² In this work, we examine the time-evolution of SWCNT chirality and local chiral angles during SWCNT growth (TE-LOCI). This is achieved *via* monitoring the average local chiral angle or LOCI of all hexagons, and its standard deviation (σ), as a function of time. It will be shown in a subsequent section that, despite its simplicity, this analysis provides detailed understanding of the growth process and the dynamics of SWCNT chirality itself. The LOCI analysis yields no information as to the *origin* of SWCNT chirality. Indeed the (as yet unknown) origin of

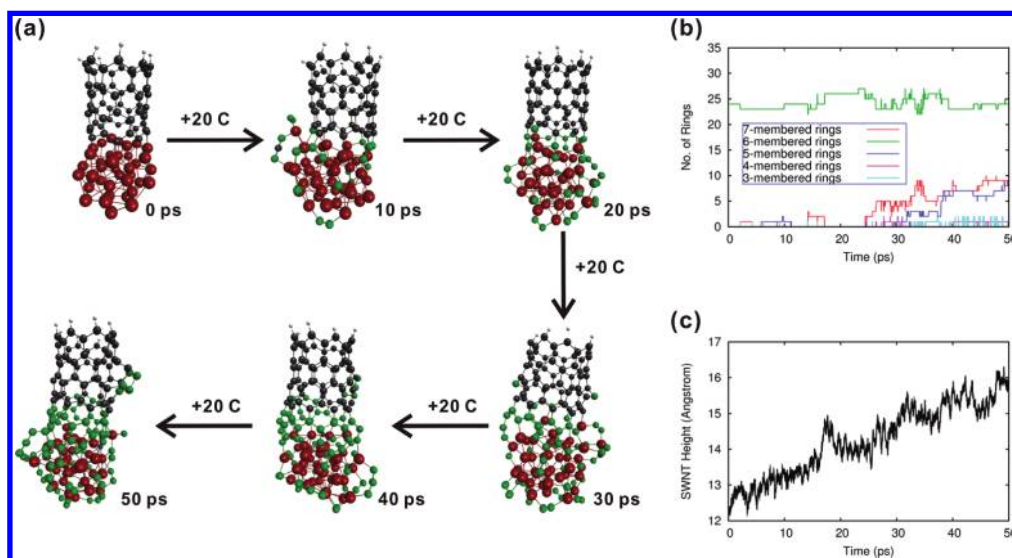


Figure 1. Fe₃₈-catalyzed “fast” growth from an (8,0)-SWCNT fragment observed in trajectory (8,0)_{fast}-I. (a) Snapshots of the QM/MD growth trajectory, showing that growth is driven by the formation of hexagonal and defective pentagonal/heptagonal carbon rings at the SWCNT–catalyst interface. In this trajectory the addition of defective rings is particularly prominent. Brown, black, white, and green spheres represent Fe, C, H, and added C atoms, respectively. (b) Polygonal carbon ring populations observed during SWCNT growth. (c) Length of the (8,0) SWCNT fragment during the first 50 ps of growth.

SWCNT chirality is still of great importance, although somewhat beyond the scope of this work. It is hoped that the application of LOCI analysis during nucleation and growth can shed light on the origin of chirality in future works.

3. RESULTS AND DISCUSSION

We have previously reported the SWCNT growth mechanism of (5,5) SWCNT fragments and “caps” on a number of occasions, as have a number of other groups (see refs 4 and 23 and references therein). Indeed, the majority of theoretical investigations of SWCNT growth typically employ (*n,n*) SWCNT caps/fragments. We therefore direct the reader to these works for a detailed discussion of (5,5) SWCNT growth. We focus here instead upon our simulations of (8,0) SWCNT growth; we believe this to be the first such QM/MD simulation reported in the literature.

3.1. (8,0) SWCNT Growth Mechanism. The growth mechanism of an illustrative trajectory (trajectory (8,0)_{fast}-I) is illustrated in Figure 1. Following adsorption onto the Fe₃₈ surface, carbon atoms almost immediately form reactive C₂ moieties (a barrierless process), which then generally reacted quickly with nearby SWCNT carbon dangling bonds (Figure 1a). Due to the stabilizing effect of the catalyst surface, the short polyyne chains thus formed were able to persist and subsequently undergo C₂ addition in turn. These extended polyyne chains easily underwent either interaction with one another, or self-isomerization, due to their high mobility on the catalyst surface. The latter is a result of both the environmental temperature (1500 K) and the relatively weak carbon–catalyst interaction. As we have observed previously, the SWCNT growth process was driven predominantly by the addition of hexagons, heptagons, and pentagons at the SWCNT base (Figure 1b) as a result of this isomerization. Ultimately, this ring addition at the SWCNT–catalyst interface resulted in the extension of the SWCNT fragment by *ca.* 3 Å during the 40 ps QM/MD simulation (Figure 1c).

While it may be tempting to compare this quantity with the simulated growth rates of (5,5) and (8,0) SWCNT fragments

(thereby furnishing an “*in situ*” measurement of chirality-dependent growth rates), such a comparison would be misleading. The artificial manner in which carbon feedstock is supplied to the SWCNT base leads to growth rates which are several orders of magnitude higher than currently established experimental data.^{32–40} This high supply rate of carbon atoms also leads to the aforementioned chaotic nature of SWCNT growth. Consequently, any trace of the original (8,0) SWCNT edge structure in these trajectories is lost almost immediately due to the formation of these defect structures that drive growth itself. In the remainder of this work, we will discuss this loss of local (*n,m*) chirality and discuss its implications in the context of chirality-dependent SWCNT growth rates.

3.2. (8,0) SWCNT Growth: Defect Healing. One method by which SWCNT chirality can be controlled during growth simulation is by limiting the rate of carbon incorporation into the SWCNT. We have previously shown the effects of such “defect-healing” in the context of (5,5) SWCNT growth on a variety of Fe-nanoparticle catalysts.^{23,29,41} In essence, a slower rate of carbon incorporation into the growing SWCNT structure allows kinetically constrained isomerization processes (i.e., pentagon/heptagon ring-opening, followed by hexagon formation) to take place in the *sp*²-hybridized carbon network. Thus, chirality controlled growth can therefore be viewed in terms of the rate of defect removal versus the rate of defect formation in the SWCNT structure.

The “slow” SWCNT growth simulations presented in this work enable us to compare the SWCNT healing processes observed during the growth of (5,5) and (8,0) SWCNTs. Thus, we can ascertain whether or not *n* and *m* bear any influence on the ability of a SWCNT to heal itself during the growth process. One such growth simulation is depicted in Figure 2 (trajectory (8,0)_{slow}-J). Comparison of this figure with Figure 1 and SI Figure S6 for (8,0)_{fast} shows a marked contrast. In the case of slow growth, as expected, the addition and retention of hexagons in the SWCNT structure is now more noticeable, compared to the case of fast growth. Admittedly, some defects are still present at 300 ps (Figure 2b). Nevertheless, a further

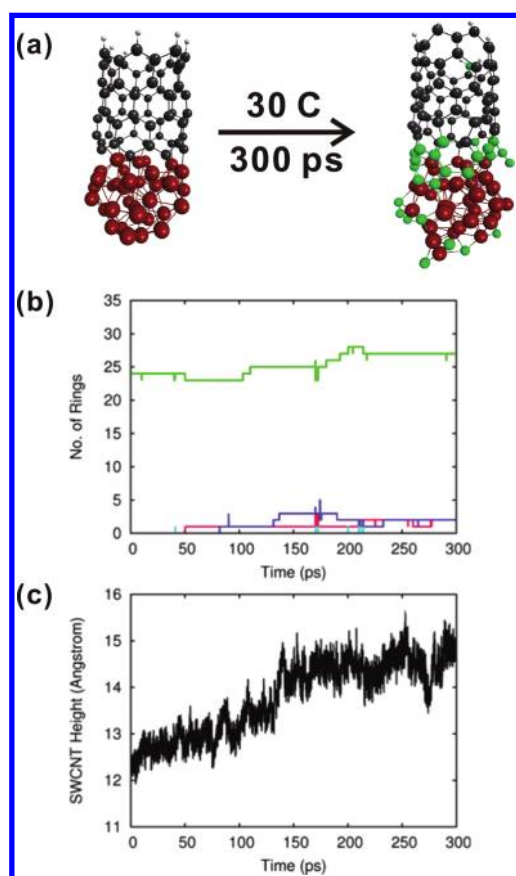


Figure 2. “Slow” SWCNT growth from an (8,0) fragment in trajectory (8,0)_{slow}-J. (a and b) In 300 ps (30 carbon atoms added) growth is driven predominantly by hexagonal rings, with pentagonal/heptagonal ring addition significantly tempered compared to fast growth (Figure 1b). Color scheme as in Figure 1. (c) Length of (8,0) SWCNT fragment during the first 300 ps of growth.

reduction of the supply rate of carbon feedstock is anticipated to remove the formation of defects during SWCNT growth altogether.²³ It is also noted with respect to Figure 2 that a slower rate of carbon supply does not reduce the “efficiency” of SWCNT growth, in a “per-carbon-atom” sense. For instance, following the addition of 30 carbon atoms, the SWCNT fragment was extended by *ca.* 0.04 Å. By comparison, the extension of the SWCNT fragment following 30 carbon atoms during “fast” growth (Figure 1 and SI Figure S6) was *ca.* 0.02 Å. An analogous, yet more dramatic, trend was observed for (5,5) SWCNT growth in a previous investigation.²⁹

To further elucidate any possible influence of (*n,m*) on the control of chirality during growth, we use the concept of “net SWCNT healing”.⁴¹ This quantity is defined in Table 1 as the difference between the total defects formed (Σ_1) and the total defects removed (Σ_2) naturally during a simulation. This is more informative than simply comparing the total number of “chirality-controlled” trajectories for (5,5) and (8,0) SWCNTs (which are both approximately the same according to the current simulations). The simulations of (5,5) SWCNT growth in this work differ from those in Table 1 only by the fact that in this work a fragment of a (5,5) SWCNT is employed, whereas those reported previously employed a curved “fullerene-like” SWCNT cap with a (5,5) edge.⁴¹ Since the defect addition/healing phenomena discussed in Table 1 pertain only to the edge structure of the SWCNT, these two sets of simulations are

Table 1. Comparison of Defect Formation and Removal during “Slow” Fe₃₈-Catalyzed Growth of (5,5) and (8,0) SWCNTs^a

		(5,5)	(8,0)
defect formation	pentagon formation	3.2	4.5
	heptagon formation	0.2	0.3
	hexagon → heptagon transformation	2.7	3.7
	hexagon → deformation	1.0	0.6
	hexagon → pentagon transformation	0.1	0.5
	total defects formed (Σ_1)	7.2	9.6
defect removal	hexagon formation	3.4	2.1
	heptagon → hexagon transformation	1.1	0.8
	pentagon → hexagon transformation	1.2	0.8
	total defects removed (Σ_2)	5.7	3.7
net healing ($\Sigma_2 - \Sigma_1$)		−1.5	−5.9

^aAll data are averaged over 10 trajectories following 300 ps of QM/MD simulation. (5,5) SWCNT data are reproduced with permission from ref 41.

in effect identical to each other in this respect. From Table 1, it is evident that the net healing of the (8,0) SWCNT fragment during slow growth is significantly inferior to that observed during equivalent simulations using a (5,5) SWCNT cap, with $\Sigma_2 - \Sigma_1$ being −5.9 (zigzag) compared to −1.5 (armchair). According to Table 1, not only is the (8,0) SWCNT prone to greater defect formation during growth, it is also less able to remove these defects once they have formed. The pronounced defect formation in this case is due almost entirely to more frequent pentagon formation and more frequent hexagon → heptagon transformation. All other phenomena associated with defect formation are comparable to those observed during the growth of the (5,5) SWCNT cap. Similarly, the inhibited defect removal in the case of (8,0) SWCNT growth is due almost completely to a slower rate of hexagon formation, compared to the case of (5,5) SWCNT growth (2.1 rings during 300 ps, as opposed to 3.4, respectively).

Thus, it is concluded that (*n,m*) does indeed bear an effect on the ability of a growing SWCNT to heal itself during growth. In particular, (5,5) SWCNTs exhibit greater averseness to defect formation, and also a greater ability to remove defects, compared to (8,0) SWCNTs. However, as we will show in the subsequent section using LOCI analysis, this does not necessarily equate to a control of the SWCNT chirality during growth. We note here that Table 1 provides no indication as to the effect of the net growth rate on the net rate of healing, and whether slower growth rates quench this trend. Nevertheless, this relationship between (*n,m*) and SWCNT healing is consistent with several previous calculations of the relative stabilities of armchair and zigzag SWCNT edge structures on transition metal catalyst nanoparticles.^{42–44} For instance, it is known that the former exhibit greater thermodynamic stability on Fe, Co, and Ni catalysts, compared to the latter. This is also the case in vacuum; the “edge energy” of (5,5) SWCNTs is known to be lower compared to that of (8,0) SWCNTs.⁴⁵ The transformation from (11,0) to (7,7) chirality of a SWCNT cap during nucleation has also been demonstrated recently during MD/Monte Carlo simulations,²¹ thereby demonstrating the relative stabilities of these two SWCNT structures.

3.3. Dynamics of Local Chirality during (5,5) SWCNT Growth. As discussed in the preceding section, “fast” SWCNT growth induces many defects into the SWCNT structure in addition to hexagons. On the other hand, “slow” SWCNT

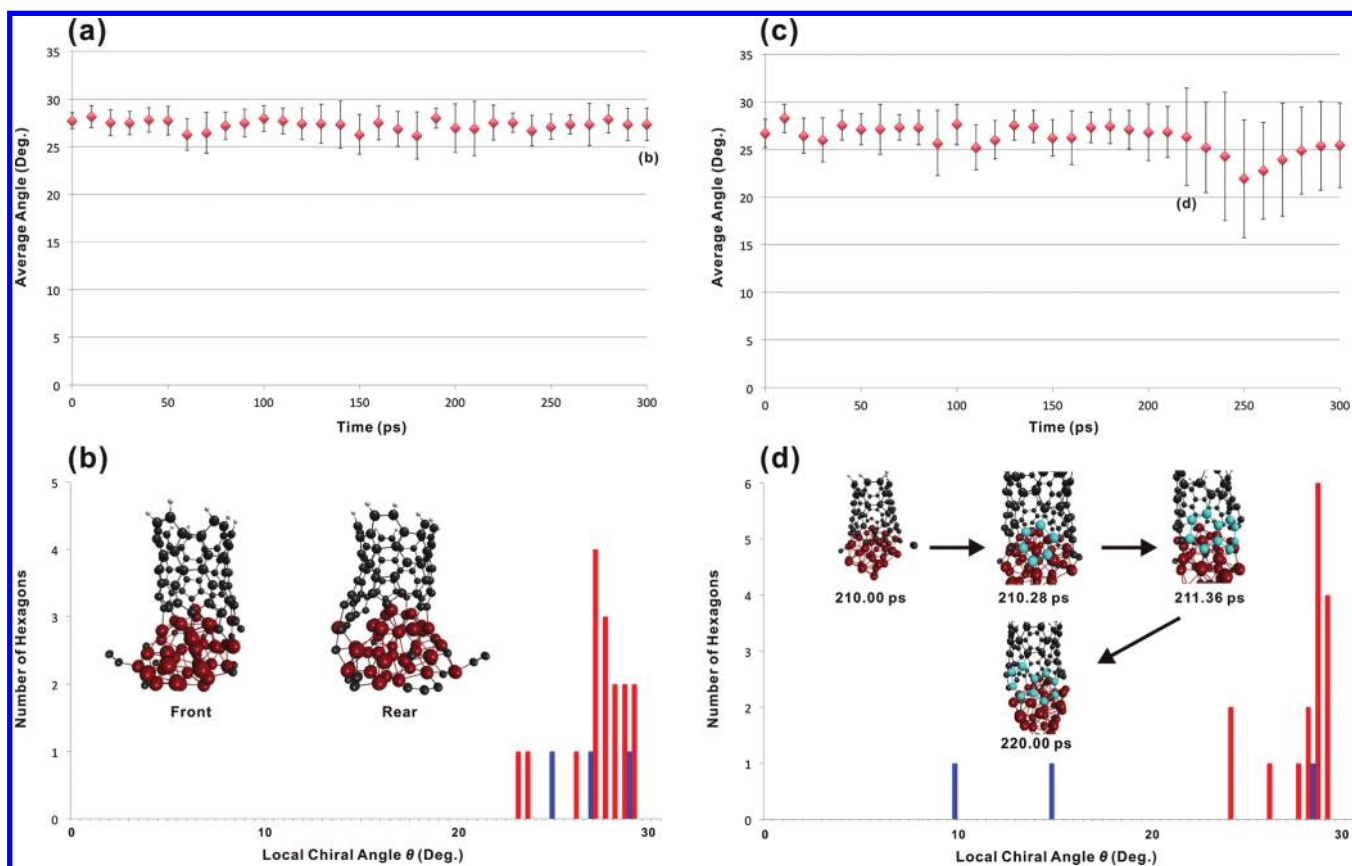


Figure 3. TE-LOCI analysis of slow $(5,5)$ SWCNT growth, demonstrating (a and b) chirality-controlled $(5,5)$ SWCNT growth observed in trajectory $(5,5)_{\text{slow-B}}$, and (c and d) a loss of $(5,5)$ SWCNT chirality during growth observed in trajectory $(5,5)_{\text{slow-F}}$. Data shown in parts a and c are average θ values; error bars denote 1σ standard deviation. (b) Local chiral angles of all hexagons in trajectory $(5,5)_{\text{slow-B}}$ at 300 ps. (d) Local chiral angles of all hexagons in trajectory $(5,5)_{\text{slow-F}}$ at 220 ps. Red and blue bars denote original and added hexagons, respectively, snapshot color scheme as in Figure 1, cyan spheres denote carbon atoms discussed in the text.

growth exhibits greater hexagon formation and, so, is more amenable to LOCI analysis. We therefore focus on “slow” SWCNT growth in the following discussion. TE-LOCI analysis of trajectory $(5,5)_{\text{slow-B}}$ (Figure 3a) shows no dramatic change in the average θ and corresponding σ , from the original chirality of the SWCNT ($(5,5)$ in this case) for the first 300 ps of growth. However, this does not indicate the success of chirality-controlled SWCNT growth, since SWCNT growth in this trajectory exhibited heptagon and pentagon defects (Figure 3b). In particular, incoming carbon atoms readily initiated hexagon \rightarrow heptagon transformation. This fact is reflected in the LOCI analysis; the total number of hexagons in the SWCNT at 300 ps (19 hexagons) was *decreased* compared to that in the initial SWCNT (20 hexagons, SI Figure S1). Such dynamic local chirality was also observed in trajectories $(5,5)_{\text{slow-C}}$, $-G$, and $-J$ (see SI Figure S7). The local chirality was retained in each of these three trajectories up to 300 ps despite the presence of defects in the SWCNT structure. Thus, it is apparent that LOCI, or TE-LOCI, analysis does not alone provide a complete description of chirality-controlled SWCNT growth. Nevertheless, LOCI is a powerful complementary tool by which deviations in local and global chiral angles can be observed during growth.

Alternatively, the local chirality can change during the growth process, a phenomenon typically indicated by a sudden change in either/both θ and/or σ (for example, such as that observed at 220 ps in trajectory $(5,5)_{\text{slow-F}}$; Figure 3c). In this case, this

sudden change was caused by the formation of a single hexagon with a significantly different local chiral angle; this hexagon was the result of an incoming carbon atom attacking a pentagon at 210.28 ps (i.e., a defect-healing process, somewhat ironically). Nevertheless, this hexagon ultimately possessed a local chiral angle that is more typical of a zigzag SWCNT ($\theta = 9.7^\circ$), since the adjacent heptagon defect was not removed. Another instance of “defective” hexagon formation was observed in this trajectory at 211.36 ps, in this case $\theta = 14.6^\circ$. Both hexagons here remained in the SWCNT structure for the remainder of the simulation. From these observations it is concluded that to accomplish chirality-controlled SWCNT growth, the *prevention* of defect formation is a key factor. Thus, chirality-controlled growth is not determined solely by the defect-healing process (such as in trajectory $(5,5)_{\text{slow-F}}$; Figure 3d) but additionally by the ability to impede defect formation in the first place. Corroborating TE-LOCI analyses of trajectories $(5,5)_{\text{slow-A}}$ and $-D$ are presented in SI Figure S8.

While sudden variations in θ and concomitant increases in σ are observed during SWCNT growth, so are the reverse processes. Such “recovery” of SWCNT chirality is illustrated in Figure 4a. In the case of trajectory $(5,5)_{\text{slow-I}}$, the average θ and σ suddenly decreased and broadened at 120 ps, respectively, only to be restored *ca.* 20 ps later. This was due to carbon atom addition into an adjoined hexagon/pentagon structure, resulting in a bridged structure that ultimately yields a hexagon with near-zigzag chirality ($\theta = 1.7^\circ$, Figure 4b). This particular

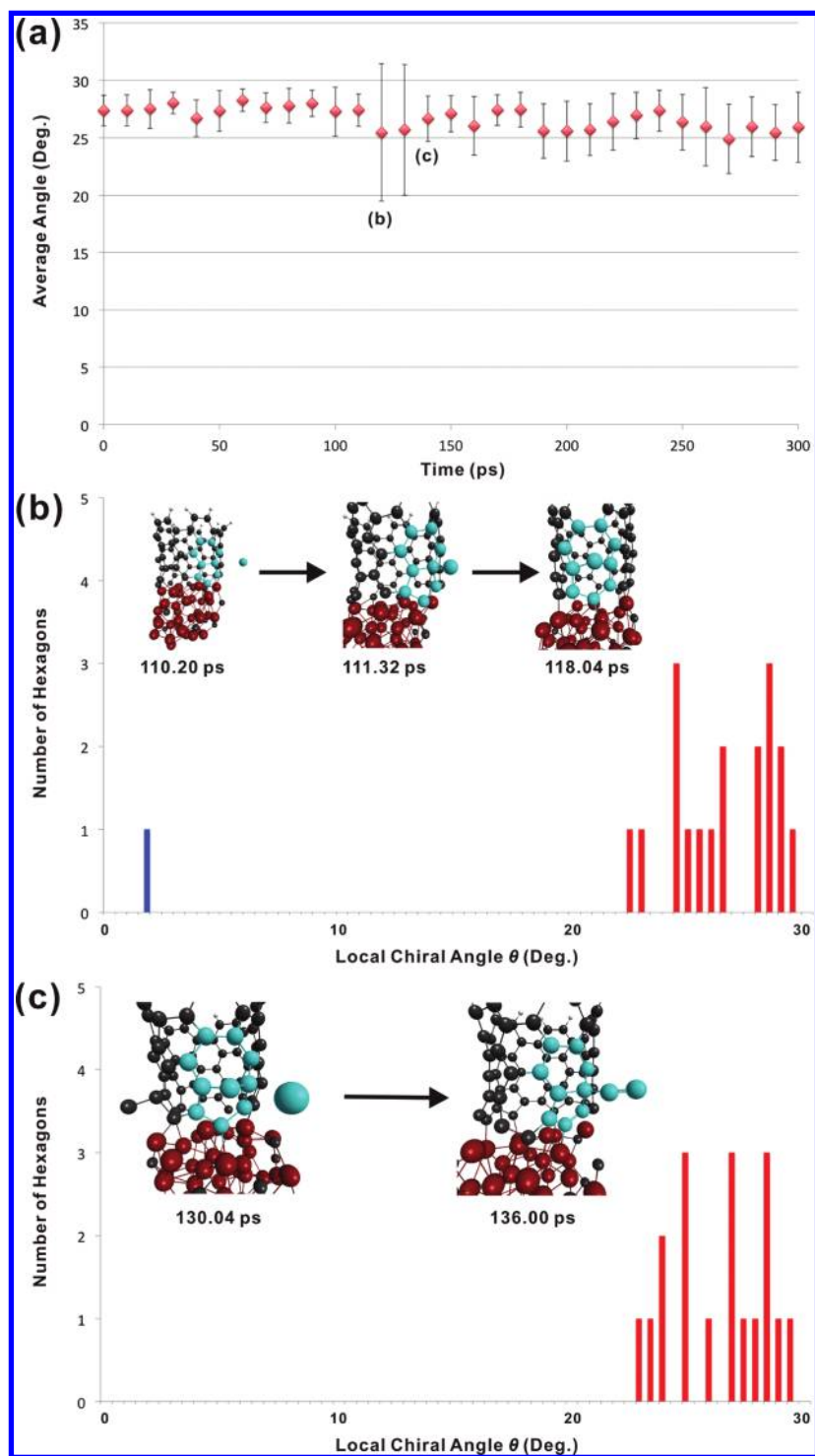


Figure 4. TE-LOCI analysis of trajectory $(5,5)_{\text{slow-I}}$, demonstrating a recovery of $(5,5)$ SWCNT chirality during growth. (a) Average θ computed using TE-LOCI analysis; error bars denote 1σ standard deviation. (b) Snapshots and local chiral angles of all hexagons at 120 ps. (c) Snapshots and local chiral angles of all hexagons at 140 ps. Color scheme as in Figure 3.

hexagon was present for only *ca.* 12 ps, however, before another incoming carbon atom induced the re-formation of a pentagon (and a single C_2 moiety) in its place. It is noted that this structural change in the growing SWCNT structure can be detected *via* a TE-LOCI analysis, despite its subtlety. Further examples of such structural transformations and changes in SWCNT chirality during growth are provided in SI Figures S9 and S10.

3.4. Dynamics of Local Chirality during $(8,0)$ SWCNT Growth. We now turn to a discussion of TE-LOCI analysis of $(8,0)$ SWCNT growth. As can be seen in Figure 5a, local chirality is preserved in trajectory $(8,0)_{\text{slow-A}}$ during growth. That is, no fluctuation in θ was observed. In addition, new hexagons exhibiting the “original” chirality of the SWCNT were added during growth. Although this trajectory shows chirality-controlled growth, at least in the context of TE-LOCI analysis,

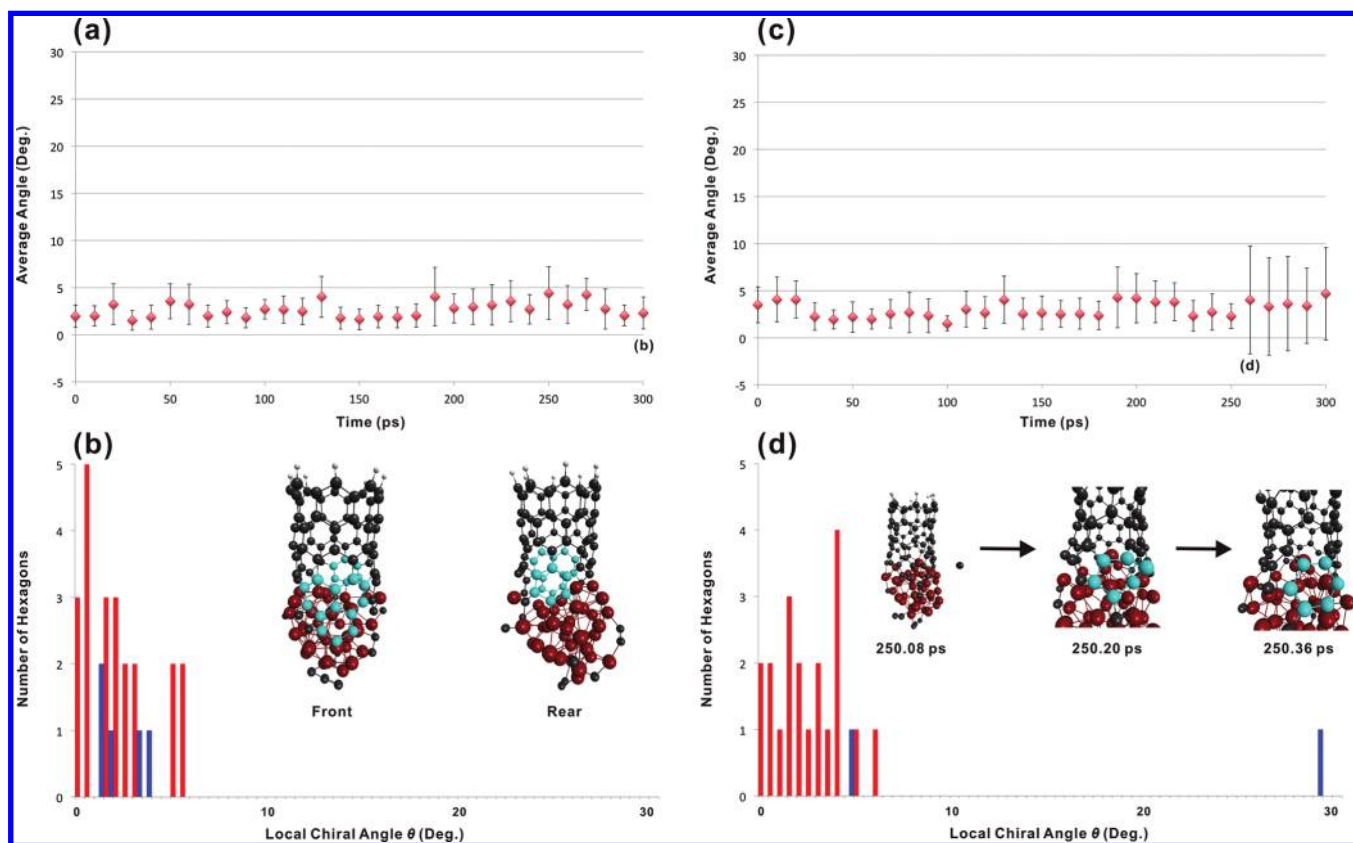


Figure 5. TE-LOCI analysis of slow (8,0) SWCNT growth, demonstrating (a and b) chirality-controlled (8,0) SWCNT growth observed in trajectory (8,0)_{slow}-A, and (c and d) a loss of (8,0) SWCNT chirality during growth observed in trajectory (8,0)_{slow}-D. Data shown in parts a and c are average θ values; error bars denote 1σ standard deviation. (b) Local chiral angles of all hexagons in trajectory (8,0)_{slow}-A at 300 ps. (d) Local chiral angles of all hexagons in trajectory (8,0)_{slow}-D at 220 ps. Color scheme as in Figure 3.

it also exhibited a defect that resulted from the destruction of preexisting hexagons, as observed also in the case of (5,5) SWCNT growth. Similar events were observed in other computed trajectories of (8,0) SWCNT growth (see Figure SI S11). Abrupt changes in the local chirality were also observed during (8,0) SWCNT growth, as in the case of (5,5) SWCNT growth. This is illustrated in Figure 5c, which depicts the TE-LOCI of trajectory (8,0)_{slow}-D. Further examples are also presented in Figure SI S12. Up until 250 ps, local chirality was conserved during growth at a value essentially equivalent to that of a pristine zigzag SWCNT. However, as shown in Figure 5d, an incoming carbon atom inserted directly into an existing pentagon defect at 260 ps, thereby creating a hexagon possessing near-armchair chirality ($\theta = 29.2^\circ$). This structure was subsequently maintained for the remainder of the simulation. It is noted that the formation of this hexagon takes place *via* a route commonly associated with defect formation, *viz.* carbon atom insertion into an existing C–C bond. Following this result, we conclude that the preservation of local chirality during growth cannot be achieved in the absence of healing processes that remove defect structures located near the SWCNT-catalyst interface. That is, healing during SWCNT growth is necessary for the conservation of local chirality.

We have thus far categorized trajectories of (8,0) and (5,5) SWCNT growth into two principal types, *viz.* those where local chirality is preserved and those where it is destroyed due to the formation of “nonzigzag”/“nonarmchair” hexagons (those with θ far from $0/30^\circ$). However, another type of growth was also

observed exclusively in the case of (8,0) SWCNTs, which is characterized by the formation of hexagons with intermediate values of θ . Figure 6 illustrates this type of growth in the case of trajectory (8,0)_{slow}-I. From Figure 6a, TE-LOCI analysis shows that σ broadened at *ca.* 160 ps due to the presence of two hexagons exhibiting local chiral angles of 16.6° and 18.0° . Interestingly, these hexagons were not newly added during the growth process, they were instead among those comprising the original SWCNT structure (Figure 6b). In this case, an incoming carbon atom was readily inserted into the preexisting hexagon, resulting in a heptagon defect at 150.36 ps. This added heptagon defect significantly distorted the adjacent hexagon, resulting in a deviation of its chiral angle from 0° . Analogous results were observed in trajectories (8,0)_{slow}-B and -H (see Figure SI S13). In all cases, all distorted hexagons resulted from the presence of an adjacent heptagon (not pentagon) defect. It is noted that no such distortion was observed in the simulation of (5,5) SWCNT growth. This result is therefore strongly related to the fact that hexagon \rightarrow heptagon transformation was observed during (8,0) SWCNT growth more frequently than during (5,5) SWCNT growth, as is shown in Table 1. Thus, the preservation of local chirality during (8,0) SWCNT growth is evidently more difficult compared to (5,5) SWCNT growth.

4. CONCLUSIONS

We have presented an analysis of the dynamics of SWCNT chirality during SWCNT growth using QM/MD simulations in conjunction with the recently developed LOCI method²² of

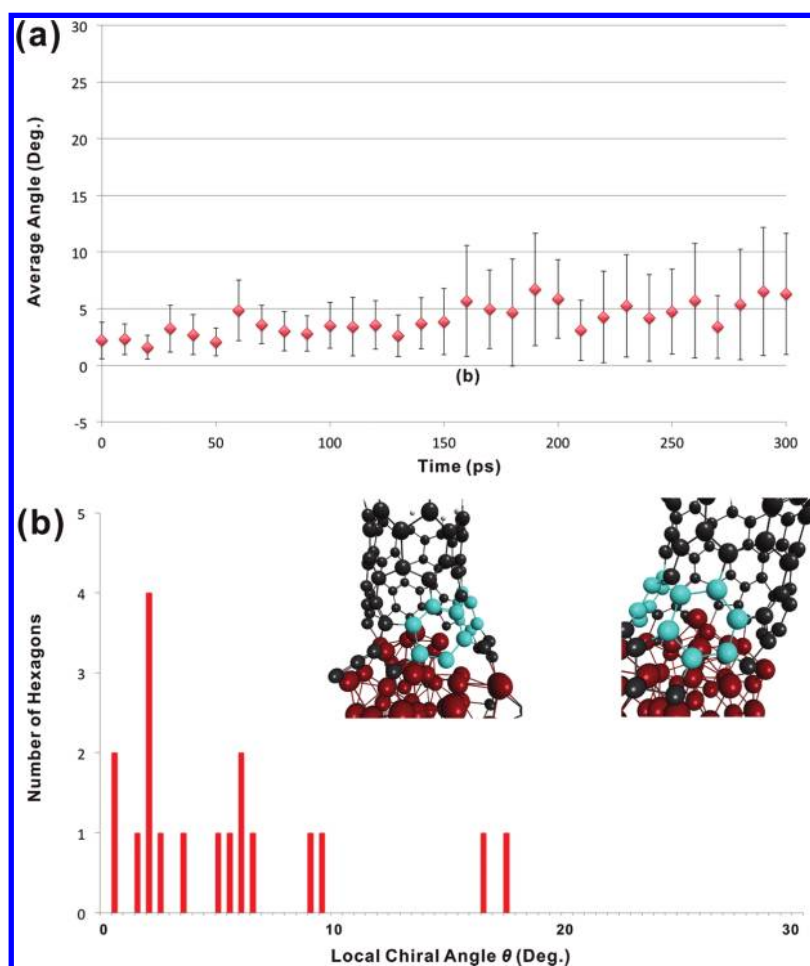


Figure 6. (a) TE-LOCI analysis for trajectory $(8,0)_{\text{slow-I}}$. Data shown are average θ values; error bars denote σ deviation. (b) Structure of trajectory $(8,0)_{\text{slow-I}}$ at 300 and its LOCI analysis at 160 ps (16 carbon atoms added). Color scheme as in Figure 3.

chiral-angle analysis. The latter is based upon the relationship between the global principal axis of the SWCNT and the local principal axis of the constituent hexagons; as such, it has a sound physical basis. QM/MD simulations of the growth of $(5,5)$ and $(8,0)$ SWCNT fragments reveal that SWCNT defect healing—the process by which defect structures such as pentagons and heptagons are removed from the SWCNT structure—is a necessary, but not sufficient, condition for chirality-controlled SWCNT growth. While defect healing results in the formation of new hexagons in the growing SWCNT, TE-LOCI analysis of the SWCNT structure suggests that the local chirality of the SWCNT edge region (and thus the chirality of the entire SWCNT) changes as a result of the defect healing process, as was recently suggested on the basis of *in situ* Raman spectroscopy.⁴⁶ This fact implies that a key factor in achieving chirality-controlled SWCNT growth is the prior prevention of defect formation during the growth process. In this respect, the presented QM/MD simulations indicate that zigzag SWCNTs are significantly inferior in maintaining their chirality during growth in comparison with armchair SWCNTs. This finding fits to the experimental observation that the fraction of zigzag- or near-zigzag-type SWCNTs is smaller than that of near-armchair SWCNTs.⁴⁷

■ ASSOCIATED CONTENT

📄 Supporting Information

Initial optimized geometries of SWCNT-Fe₃₈ molecular structures, polygonal ring population analyses, and extended TE-LOCI analyses of QM/MD $(5,5)$ and $(8,0)$ SWCNT growth simulations. This material is available free of charge via the Internet at <http://pubs.acs.org>.

■ AUTHOR INFORMATION

Corresponding Author

sirle@iar.nagoya-u.ac.jp; morokuma@fukui.kyoto-u.ac.jp

Author Contributions

[†]These authors contributed equally.

Notes

The authors declare no competing financial interest.

■ ACKNOWLEDGMENTS

This work was in part supported by a CREST (Core Research for Evolutional Science and Technology) grant in the Area of High Performance Computing for Multiscale and Multiphysics Phenomena from the Japanese Science and Technology Agency (JST). S.I. also acknowledges support from the Ministry of Education, Culture, Sports, Science and Technology (MEXT) of Japan under the Strategic Programs for Innovative Research (SPIRE) and the Computational Materials Science Initiative (CMSI). Computer simulations were performed using the

Academic Center for Computing and Media Studies (ACCMS) at Kyoto University. J.K. and A.J.P. acknowledge the Fukui Fellowship of Kyoto University.

■ REFERENCES

- (1) Iijima, S. *Nature* **1993**, 363, 603.
- (2) Bethune, D. S.; Kiang, C. H.; DeVries, M. S.; Gorman, G.; Savoy, R.; Beyers, R. *Nature* **1993**, 363, 605.
- (3) Saito, R.; Fujita, M.; Dresselhaus, G.; Dresselhaus, M. S. *Phys. Rev. B* **1992**, 46, 1804.
- (4) Tessonier, J.-P.; Su, D. S. *ChemSusChem* **2011**, 4, 824.
- (5) Zhang, Y.; Zheng, L. *Nanoscale* **2010**, 2, 1919.
- (6) Cheng, H. M.; Li, F.; Sun, X.; Brown, S. D. M.; Pimenta, M. A.; Marucci, A.; Dresselhaus, G.; Dresselhaus, M. S. *Chem. Phys. Lett.* **1998**, 289, 602.
- (7) Nikolaev, P.; Bronikowski, M. J.; Bradley, R. K.; Rohmund, F.; Colbert, D. T.; Smith, K. A.; Smalley, R. E. *Chem. Phys. Lett.* **1999**, 313, 91.
- (8) Journet, C.; Maser, W. K.; Bernier, P.; Loiseau, A.; Lamy de la Chapelle, M.; Lefrant, S.; Deniard, P.; Lee, R.; Fischer, J. E. *Nature* **1997**, 388, 756.
- (9) Guo, T.; Nikolaev, P.; Rinzler, A. G.; Tomanek, D.; Colbert, D. T.; Smalley, R. E. *J. Phys. Chem.* **1995**, 99, 10694.
- (10) Thess, A.; Lee, R.; Nikolaev, P.; Dai, H.; Petit, P.; Robert, J.; Xu, C.; Lee, Y. H.; Kim, S. G.; Rinzler, A. G.; Colbert, D. T.; Scuseria, G. E.; Tomanek, D.; Fischer, J. E.; Smalley, R. E. *Science* **1996**, 273, 483.
- (11) Wang, Y.; Kim, M. J.; Shan, H.; Kittrell, C.; Fan, H.; Ericson, L. M.; Hwang, W.-F.; Arepalli, S.; Hauge, R. H.; Smalley, R. E. *Nano Lett.* **2005**, 5, 997.
- (12) Xu, Y.-Q.; Flor, E.; Schmidt, H.; Smalley, R. E.; Hauge, R. H. *Appl. Phys. Lett.* **2006**, 89, 123116/1.
- (13) Yao, Y.; Feng, C.; Zhang, J.; Liu, Z. *Nano Lett.* **2009**, 9, 1673.
- (14) Fort, E. H.; Scott, L. T. *J. Mater. Chem.* **2011**, 21, 1373.
- (15) Li, H.; Page, A. J.; Irle, S.; Morokuma, K. *ChemPhysChem* **2012**, 13, 1479.
- (16) Omachi, H.; Matsuura, S.; Segawa, Y.; Itami, K. *Angew. Chem., Int. Ed.* **2010**, 49, 10202.
- (17) Omachi, H.; Segawa, Y.; Itami, K. *Org. Lett.* **2011**, 13, 2480.
- (18) Scott, L. T.; Jackson, E. A.; Zhang, Q. Y.; Steinberg, B. D.; Bancu, M.; Li, B. *J. Am. Chem. Soc.* **2012**, 134, 107.
- (19) Gomez-Gualdron, D. A.; Zhao, J.; Balbuena, P. B. *J. Chem. Phys.* **2011**, 134, 014705.
- (20) Neyts, E. C.; Shibuta, Y.; van Duin, A. C. T.; Bogaerts, A. *ACS Nano* **2010**, 4, 6665.
- (21) Neyts, E. C.; van Duin, A. C. T.; Bogaerts, A. *J. Am. Chem. Soc.* **2011**, 133, 17225.
- (22) Kim, J.; Irle, S.; Morokuma, K. *Phys. Rev. Lett.* **2011**, 107, 175505.
- (23) Page, A. J.; Ohta, Y.; Irle, S.; Morokuma, K. *Acc. Chem. Res.* **2010**, 43, 1375.
- (24) Elstner, M.; Porezag, D.; Jungnickel, G.; Elsner, J.; Haugk, M.; Frauenheim, T.; Suhai, S.; Seifert, G. *Phys. Rev. B* **1998**, 58, 7260.
- (25) Swope, W. C.; Andersen, H. C.; Berens, P. H.; Wilson, K. R. *J. Chem. Phys.* **1982**, 76, 637.
- (26) Zheng, G.; Witek, H. A.; Bobadova-Parvanova, P.; Irle, S.; Musae, D. G.; Prabhakar, R.; Morokuma, K.; Lundberg, M.; Elstner, M.; Kohler, C.; Frauenheim, T. *J. Chem. Theor. Comput.* **2007**, 3, 1349.
- (27) Martyna, G. J.; Klein, M. L.; Tuckerman, M. *J. Chem. Phys.* **1992**, 97, 2635.
- (28) Ohta, Y.; Okamoto, Y.; Irle, S.; Morokuma, K. *J. Phys. Chem. C* **2009**, 113, 159.
- (29) Page, A. J.; Ohta, Y.; Okamoto, Y.; Irle, S.; Morokuma, K. *J. Phys. Chem. C* **2009**, 113, 20198.
- (30) Page, A. J.; Irle, S.; Morokuma, K. *J. Phys. Chem. C* **2010**, 114, 8206.
- (31) <http://kmweb.fukui.kyoto-u.ac.jp>.
- (32) Geohegan, D. B.; Puzos, A. A.; Styrer-Barnett, D.; Hu, H.; Zhao, B.; Cui, H.; Rouleau, C. M.; Eres, G.; Jackson, J. J.; Wood, R. F.; Pannala, S.; Wells, J. C. *Phys. Status Solidi B* **2007**, 244, 3944.
- (33) Sharma, R.; Rez, P.; Treacy, M. M. J.; Stuart, S. J. *J. Electron Microsc.* **2005**, 54, 231.
- (34) Xiang, R.; Einarsson, E.; Okawa, J.; Miyauchi, Y.; Maruyama, S. *J. Phys. Chem. C* **2009**, 113, 7511.
- (35) Futaba, D. N.; Hata, K.; Yamada, T.; Mizuno, K.; Yumura, M.; Iijima, S. *Phys. Rev. Lett.* **2005**, 95, 056104/1.
- (36) Yao, Y.; Liu, R.; Zhang, J.; Jiao, L.; Liu, Z. *J. Phys. Chem. C* **2007**, 111, 8407.
- (37) Bonard, J.-M.; Croci, M.; Conus, F.; Stockli, T.; Chatelain, A. *Appl. Phys. Lett.* **2002**, 81, 2836.
- (38) Puzos, A. A.; Geohegan, D. B.; Schittenhelm, H.; Fan, X.; Guillorn, M. A. *Appl. Surf. Sci.* **2002**, 197–198, 552.
- (39) Puzos, A. A.; Geohegan, D. B.; Jesse, S.; Ivanov, I. N.; Eres, G. *Appl. Phys. A: Mater. Sci. Process.* **2005**, 81, 223.
- (40) Kim, K.-E.; Kim, K.-J.; Jung, W. S.; Bae, S. Y.; Park, J.; Choi, J.; Choo, J. *Chem. Phys. Lett.* **2005**, 401, 459.
- (41) Page, A. J.; Chandrakumar, K. R. S.; Wang, Y.; Irle, S.; Morokuma, K. In *Electronic Properties of Carbon Nanotubes*; Maruland, J. M., Ed.; InTech: Rijeka, Croatia, 2011.
- (42) Ding, F.; Harutyunyan, A. R.; Yakobson, B. I. *Proc. Natl. Acad. Sci.* **2009**, 106, 2506.
- (43) Reich, S.; Li, L.; Roberson, J. *Chem. Phys. Lett.* **2006**, 421, 469.
- (44) Börjesson, A.; Bolton, K. *ACS Nano* **2011**, 5, 771.
- (45) Liu, Y.; Dobrinsky, A.; Yakobson, B. I. *Phys. Rev. Lett.* **2010**, 105, 235502.
- (46) Picher, M.; Navas, H.; Arenal, R.; Quesnel, E.; Anglaret, E.; Jourdain, V. *Carbon* **2012**, 50, 2407.
- (47) Rao, R.; Liptak, D.; Cherukuri, T.; Yakobson, B. I.; Maruyama, B. *Nat. Mater.* **2012**, 11, 213.